Numerical Investigation of a Fuel Cell-Powered Agricultural Tractor

energies

MDPI

Article

Numerical Investigation of a Fuel Cell-Powered Agricultural Tractor

Valerio Martini †, Francesco Mocera *,† and Aurelio Somà †

Department of Mechanical and Aerospace Engineering, Politecnico di Torino, Corso Duca degli Abruzzi 24, 10129 Torino, Italy; valerio.martini@polito.it (V.M.); aurelio.soma@polito.it (A.S.)

* Correspondence: francesco.mocera@polito.it; Tel.: +39-011-090-5177

† These authors contributed equally to this work.

Abstract: In recent years, growing awareness about environmental issues is pushing humankind to explore innovative technologies to reduce the anthropogenic sources of pollutants. Among these sources, internal combustion engines in non-road mobile machinery (NRMM), such as agricultural tractors, are one of the most important. The aim of this work is to explore the possibility of replacing the conventional diesel engine with an electric powertrain powered by a hybrid storage system, consisting of a small battery pack and a fuel-cell system. The battery pack (BP) is necessary to help the fuel cell manage sudden peaks in power demands. Numerical models of the conventional powertrain and a fuel-cell tractor were carried out. To compare the two powertrains, work cycles derived from data collected during real operative conditions were exploited and simulated. For the fuel-cell tractor, a control strategy to split the electric power between the battery pack and the fuel cell was explored. The powertrains were compared in terms of greenhouse gas emissions (GHG) according to well-to-wheel (WTW) equivalent CO_2 emission factors available in the literature. Considering the actual state-of-the-art hydrogen production methods, the simulation results showed that the fuel-cell/battery powertrain was able to accomplish the tasks with a reduction of about 50% of the equivalent CO_2 emissions compared to traditional diesel-powered vehicles.

Keywords: agricultural machinery; NRMM; fuel cell; hydrogen; innovative powertrain; hybrid storage system; GHG emissions reduction; hybrid electric tractor

Citation: Martini, V.; Mocera, F.; Somà, A. Numerical Investigation of a Fuel Cell-Powered Agricultural Tractor. *Energies* **2022**, *15*, 8818. https://doi.org/10.3390/en15238818

Academic Editors: Mario Marchesoni, Xianke Lin and Jamie W.G. Turner

Received: 11 October 2022
Accepted: 18 November 2022
Published: 22 November 2022

1. Introduction

Growing awareness about environmental pollution has forced many governments and institutions to tighten the stringent limits on engine exhaust emissions. Among the various anthropic sources of pollutants, agricultural tractors, traditionally equipped with compression ignition engines, play an important role. The agricultural sector is, according to estimations, responsible for almost 20% of the annual global production of CO_2 emissions [1]. In addition, the internal combustion engine produces other harmful products, such as NOx, CO, particulate matter (PM) and hydrocarbons (HC). Consequently, strict emission regulations have been recently imposed also on the sector of non-road mobile machinery (NRMM) [2]. To reduce the emissions, and thus be compliant with the severe regulations, several techniques regarding exhaust gas aftertreatment systems have been proposed [3]. Other studies have concentrated on the use of alternative fuels, such as biogas and biodiesel [4–8]. However, even if biodiesel and biogas are more environmentally friendly fuels with respect to petroleum diesel, they generally do not completely overcome the problems related to emissions and, in some cases, their use causes a reduction in terms of peak power and powertrain performance [9]. Therefore, other studies [10–14] have focused on the hybridization of the powertrain, replacing the traditional diesel engine with a downsized engine and one or more electric machines. These studies showed good fuel savings, ranging from 10 to 25%, compared to traditional tractors, without significant

reductions in terms of peak power performance. However, with hybridization it is not possible to completely remove engine emissions, since the thermal unit is still producing harmful products deriving from combustion. Fully electric tractor configurations can be considered in those cases when the thermal engine needs to be removed [15,16]. The main drawbacks preventing a wider adoption of fully electric tractor configurations are related to the long expected operating time, which would require bulky battery packs, and to the long charging time, which in most cases could significantly limit the productivity of the vehicle. Therefore, current state-of-the-art battery storage systems are preventing the diffusion of pure battery electric tractors. To overcome the problems related to pure electric tractors and, at the same time, to completely remove the internal combustion engine, an alternative solution is the adoption of fuel cells. Fuel-cell powertrains have already been investigated for vehicular applications regarding passenger cars, buses and trucks [17–20]. Fuel cells can produce continuous electric current from the conversion of the chemical energy of hydrogen and oxygen through redox reactions. Presently, hydrogen is mainly derived from fossil fuels, with about half of the production obtained through steam methane reforming [21]. However, hydrogen production from renewable and clean energy sources, such as through biological conversion or biomass gasification, is gradually playing a more relevant role [22,23]. Fuel cells are characterized by higher power generation efficiencies compared to internal combustion engines, and they do not produce pollutants at the exhaust. However, fuel cells alone cannot follow the almost instantaneous changes in external load; therefore, they must operate in combination with other storage systems, such as ultracapacitors and batteries [24]. A well-known problem related to intense changes in current density of the fuel cell is gas starvation, which could lead to a reduction in the lifetime of the system [25]. The use of multiple energy sources increases the complexity of the system and, to improve the overall efficiency of the powertrain, requires the development of a proper energy-management strategy [26]. In the literature, some studies have been carried out focusing on agricultural machineries with fuel cells [27–29]; however, a deeper investigation is required, in particular with a view to greenhouse gas (GHG) emission reduction. The present paper summarizes the results of a numerical investigation of a hybrid fuel-cell/battery powertrain for agricultural tractors and is organized as follows: Section 2 contains a brief overview of the case study, a conventional diesel-powered specialized agricultural tractor which was monitored in the field during daily activities, Section 3 describes the layout of the proposed fuel-cell tractor and provides a description of the numerical modeling for the simulations, Section 4 describes and analyses the simulation results.

2. Case Study Description

2.1. Conventional Diesel Tractor

This paper focuses on a specialized agricultural tractor, namely an orchard tractor (Figure 1). This class of agricultural machines is characterized by a great compactness, since these vehicles must be able to operate among narrow rows and in small working spaces, thus must have good curving capabilities. The characteristics of the conventional diesel-powered orchard tractor used as a reference in this work are shown in Table 1.

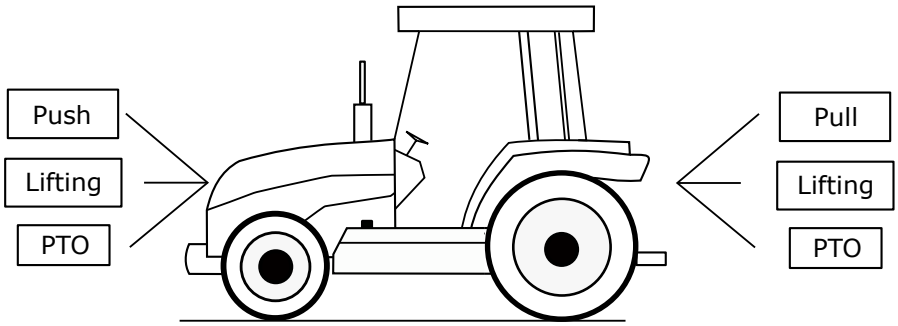

Figure 1. Schematic representation of an orchard tractor and its main duties.

Table 1. Main characteristics of the orchard tractor.

Vehicle Properties	
Mass	2571 kg
Vehicle wheelbase	1900 mm
Track width	1850 mm
Wheel radius	680 mm
Nominal power	73 kW @ 2600 rpm
Top speed	42 km/h

The internal combustion engine must provide power both for traction and for the activation of attached implements. These attached implements are generally powered by the engine through the power take-off (PTO). The vehicle considered in this study is powered by a diesel engine with a rated power of 73 kW. However, analyzing the most common working scenarios and their distribution along the year, it is possible to assert that they require significantly lower power to be accomplished. This translates into a suboptimal resulting efficiency and into excessive fuel waste. Figure 2 shows the power and torque curves of the conventional diesel engine considered in this work. These curves were derived from data available online for a commercial diesel unit with characteristics very similar in terms of power and torque.

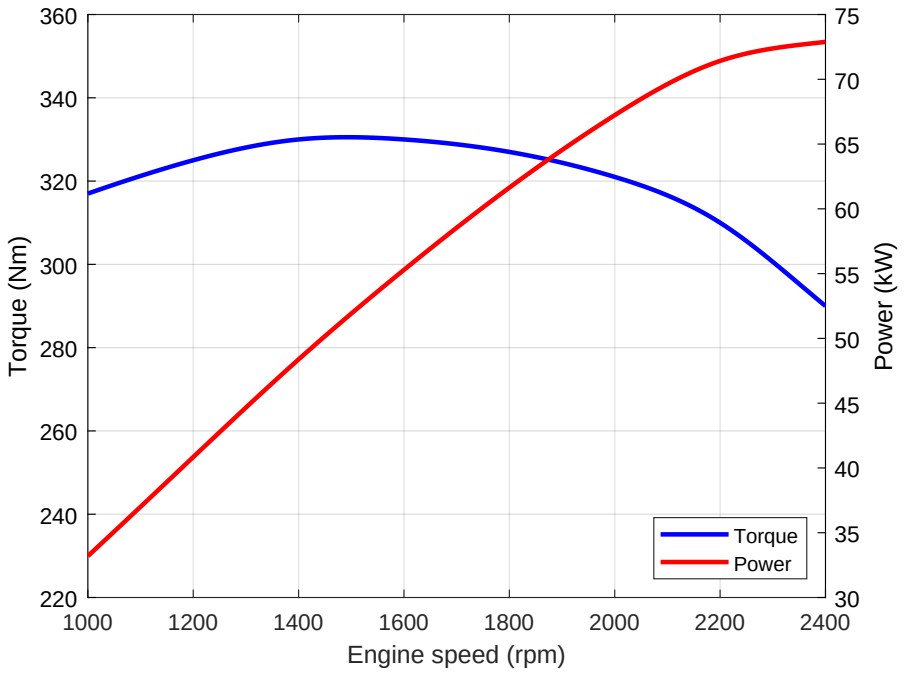

Figure 2. Torque and power curves of the conventional diesel engine.

Another key element for this class of vehicles is the gearbox. Agricultural tractor gearboxes are well known for the high number of gear ratios they can provide (Figure 3). Having a high number of gear ratios allows the driver to have the full power of the engine at different vehicle speeds, according to the task to be accomplished. The gearbox of the conventional vehicle considered in this work allows for a total of 32 gear ratios—16 forward and 16 reverse.

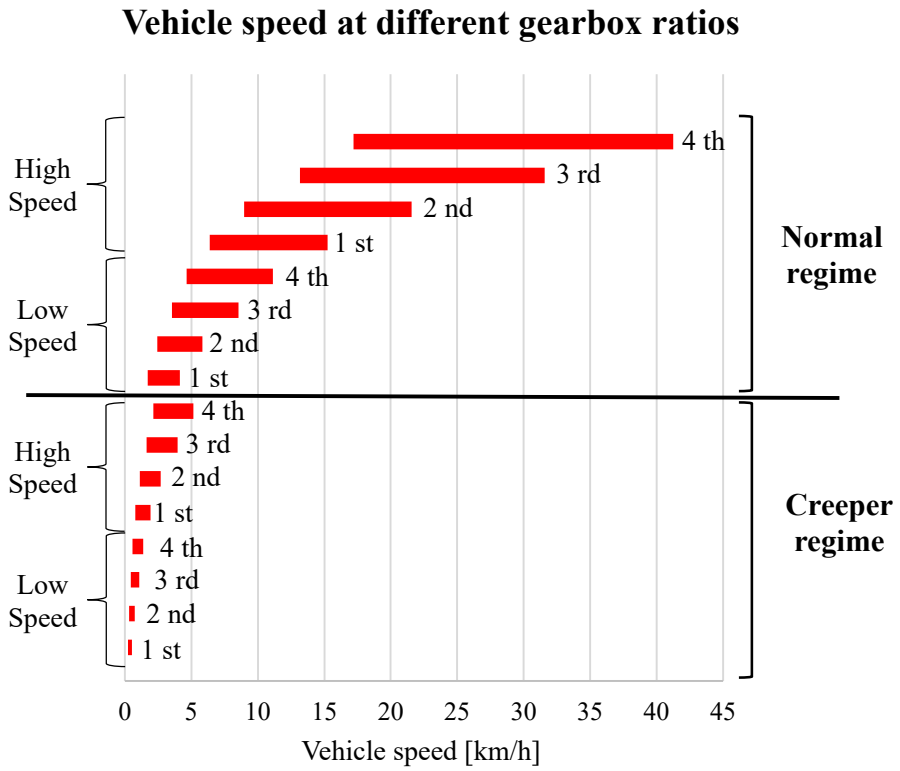

Figure 3. Typical speed distribution according to gearbox ratios.

2.2. Experimental Definition of Mission Profiles

Since tractors are multi-purpose machines, to characterize the tractor daily activities, the attention focused on monitoring engine data and driver commands through the CAN BUS network [30,31]. Data were collected from the CAN BUS network using a specifically programmed data acquisition able to take a complete picture of the state variables of the tractor every 50 ms. The attention mainly focused on monitoring the following parameters:

- Driver pedal signal as reference of the desired working speed.
- Engine rotational speed.
- Actual engine load as estimated by the vehicle control unit.
- Vehicle speed.
- PTO activation.

The data acquisition system was also provided with a GPS. Data were collected during normal daily work activities performed in northern Italy and the tests were not pre-defined for this research to avoid undesired bias from the users. Two work activities were recorded—one regarding the use of a sprayer and the other regarding the use of a weeder. Figure 4 shows the vehicle speed, the engine load and the PTO activation profiles during the weeding work cycle.

It is possible to define three main operative conditions: idle condition (0–500 s), field work activity (670–1480 s and 1680–4647 s) and vehicle traveling on the road (500–670, from the farm to the field, and 1480–1680 s, from one field to another). During the work activity on the field, the average engine load was about 25% and therefore the engine operated with a low overall efficiency. Figure 5 shows the experimental data for the sprayer work cycle. As with the weeding cycle, it is possible to highlight the same three main operating conditions. In this case, the average engine load during the field work activity was slightly above 60%. Figure 6 shows the GPS experimental data for the two work cycles.

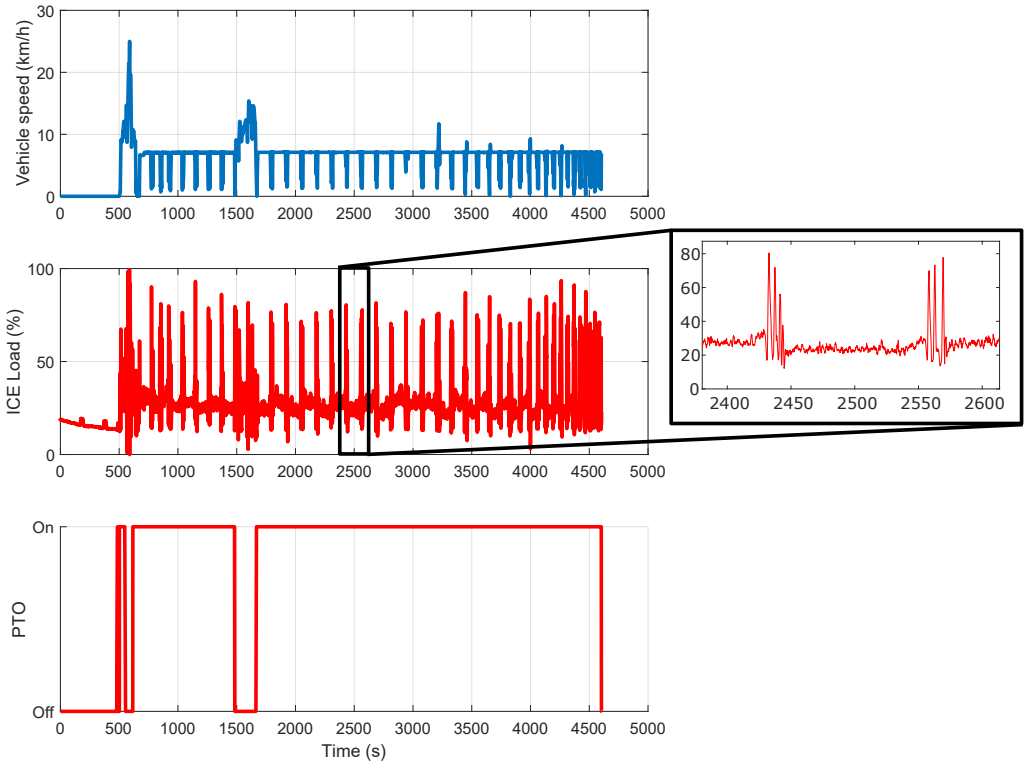

Figure 4. Experimental data for the weeding work cycle.

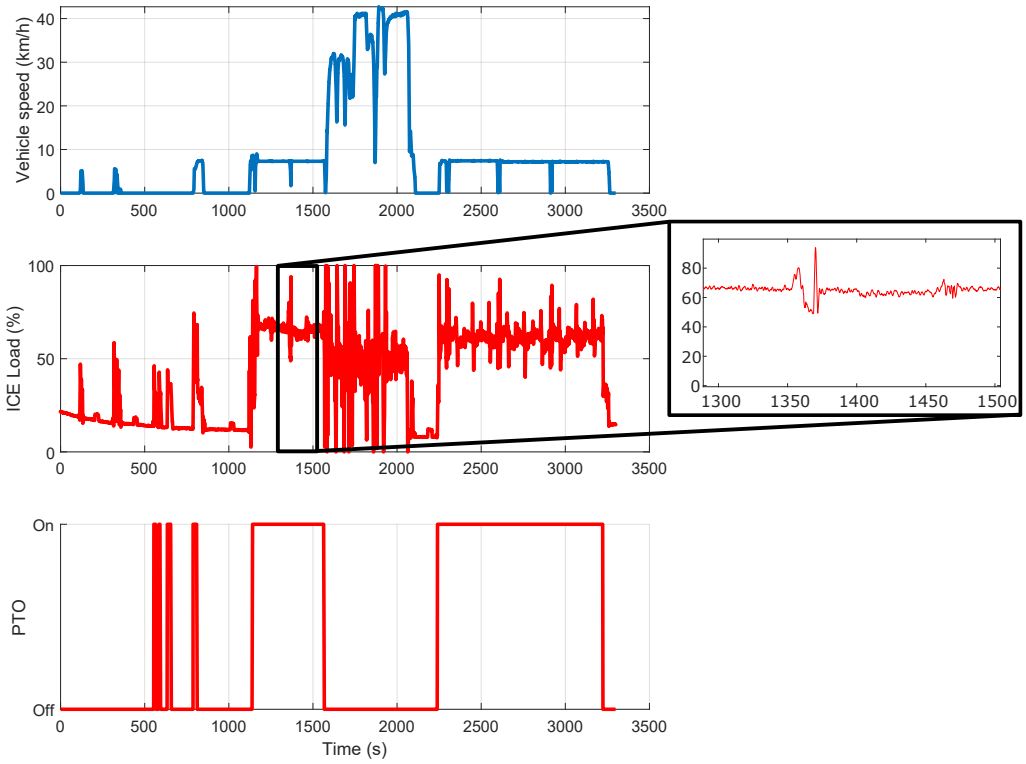

Figure 5. Experimental data for the sprayer work cycle.

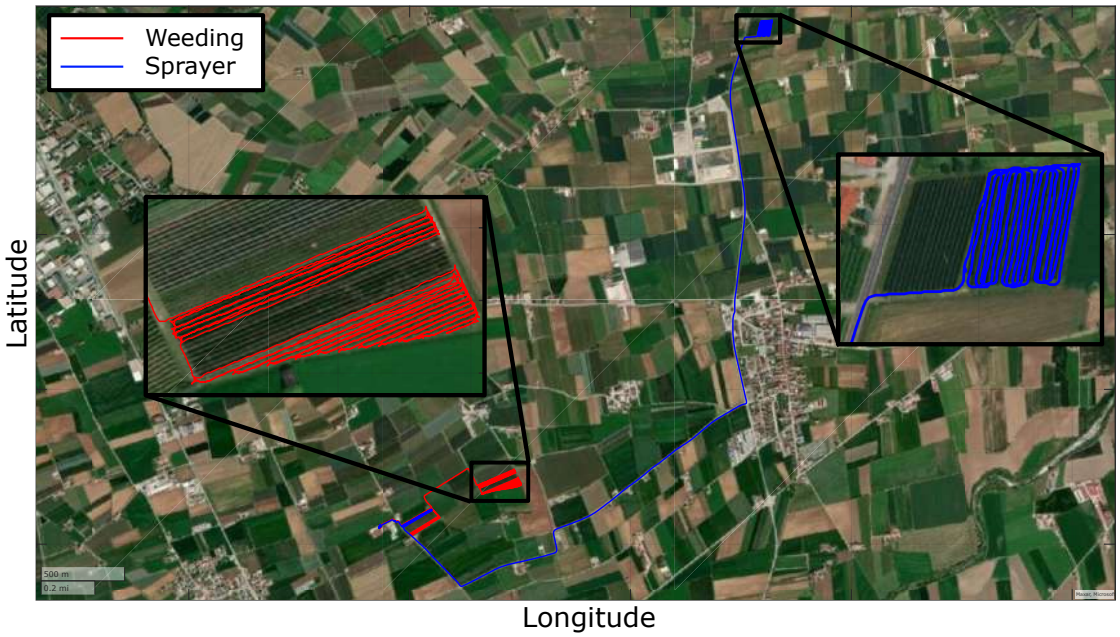

Figure 6. GPS Experimental data for the work cycles.

3. Numerical Modeling

In this section, the numerical modeling of the powertrains is explained. The software used for the simulations is Simulink, a MATLAB-based graphical programming environment developed by MathWorks (The MathWorks Inc., Natick, MA, USA). Both the traditional diesel powertrain and the hybrid fuel-cell/battery powertrain were modeled, simulated using the physical network approach [10] and compared in terms of power capabilities and fuel economy. The traditional diesel powertrain numerical model was validated comparing the simulation results with the experimental data.

3.1. Traditional Diesel Vehicle Numerical Model

As for the traditional vehicle, the following aspects were covered during the numerical modeling:

- Vehicle dynamics.
- Gearbox and clutch.
- Engine power output and fuel consumption.
- PTO and auxiliaries (AUX) loads.

The vehicle dynamics was described using a 1D longitudinal model [10–12] and was characterized by the following equations:

$$m\dot{V}_x = 2(F_{xf} + F_{xr}) - F_d - mg \cdot sin(\beta) \quad (1)$$

$$F_{zf} = \frac{-h(F_d + mg \cdot sin\beta) + b \cdot mg \cdot cos(\beta)}{2(a+b)} \quad (2)$$

$$F_{zr} = \frac{+h(F_d + mg \cdot sin\beta) + a \cdot mg \cdot cos(\beta)}{2(a+b)} \quad (3)$$

where:

- a, b, and h represent the relative position of the center of gravity of the vehicle with respect to the front and rear axles.
- m is the tractor mass, g the acceleration of gravity.
- β is the road slope angle.

- V_x is the vehicle longitudinal speed.
- F_d is the aerodynamic drag force as $F_d = 0.5\rho C_d A {V_x}^2 sign(V_x)$, with ρ the air density, C_d the drag coefficient and A the frontal cross-sectional area of the vehicle.
- F_{xf} and F_{xr} are the contact forces between the wheels and the ground on the longitudinal direction (front and rear axle).
- F_{zf} and F_{zr} are the normal contact forces between the wheels and the ground (front and rear axle).

The longitudinal model considers the vehicle motion as a result of all the relevant forces and torques applied on the tractor body. To simulate the presence of an attached trailer/implement to the tractor, a rigid connection was considered between the two bodies to share the same longitudinal speed. Therefore, during the simulations, the global mass was considered. The contact between the tires and the soil was parameterized in terms of static and kinetic coefficients. The first determines the applied torque at which the tire loses traction and begins to slip, and the second determines the amount of torque the tire transmits to the pavement once it begins to slip. The trailer tires were modeled considering different values in terms of rolling radius and rolling resistance with respect to the tractor tires. As for the gearbox, it was modeled using groups of simple gears connected in series or in parallel with the help of disengaging friction clutches to achieve the desired gear ratio. Each pair of gears was characterized by a transmission efficiency. Moreover, every element of the transmission was modeled considering reasonable values in terms of inertia and damping. The engine power output was modeled through a tabulated torque data approach using the curves shown in Figure 2. As for the fuel consumption, the engine map was obtained using a consumption model available in the literature [32]. According to this model, the brake-specific fuel consumption (BSFC) is evaluated using a polynomial curve that is a function of engine speed and torque:

$$Z = b_1 + b_2 \cdot X + b_3 \cdot Y + b_4 \cdot X^2 + b_5 \cdot X \cdot Y + b_6 \cdot Y^2 \quad (4)$$

where:

- X is the normalized engine speed: $X = \dfrac{n}{n_{nom}} \cdot 100.$
- Y is the normalized brake torque: $Y = \dfrac{T}{T_{nom}} \cdot 100.$
- Z is the normalized BSFC: $Z = \dfrac{BSFC}{BSFC_{min}} \cdot 100.$
- $b_{i=1,\ldots,6}$ are the polynomial coefficients.

According to this model, the region of minimum BSFC is usually located at about 73–77% of the nominal engine rotational speed and at high load, specifically 85–95% of the nominal torque. Lastly, the PTO and AUX loads were modeled through a resistive torque applied to the tractor. The PTO load represented the power required by the implements connected to the tractor, while the AUX load accounted for the power required by auxiliaries and accessories.

3.2. Hybrid Fuel-Cell/Battery Powertrain Numerical Model

Fuel-cell hybrid electric vehicles (FCHEVs) can be classified into different topologies. According to the classification described in [26], the proposed tractor can be defined as a fuel-cell + battery vehicle with direct parallel connection of the battery. Going into detail, the fuel cell is connected to the bus DC through a unidirectional DC–DC converter, while the battery is directly connected to the bus. In this configuration, the bus voltage is entirely determined by the battery's terminal voltage, and the fuel-cell system can be controlled through the converter, allowing for the reduction of its power fluctuations. A schematic representation of the electric configuration of the system is shown in Figure 7.

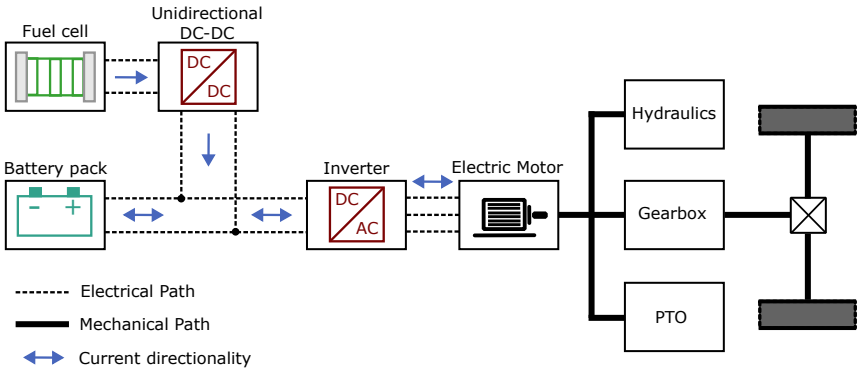

Figure 7. Schematic representation of the hybrid fuel-cell/battery powertrain.

The electric motor (EM) is then connected to the gearbox and the PTO, thus it delivers power both for traction and to the attached implements. The main properties of the EM are shown in Table 2 and were considered to be close as possible to the nominal characteristics of the diesel engine of the conventional vehicle under investigation. The electric motor efficiency was modeled using a tabulated map function of torque and speed.

Table 2. Main properties of the electric motor.

Electric Motor Properties	
Rated power	75 kW @ 2600 rpm
Rated torque	258 Nm
Maximum efficiency	94%

To preserve the performance of the conventional powertrain, the gearbox configuration was the same as the traditional vehicle.

3.2.1. Fuel-Cell Model

The fuel-cell stack voltage was modeled using the following equation:

$$V_{stack} = N_{cell} \cdot (V_{Nernst} - V_{act} - V_{ohm} - V_{conc}) \quad (5)$$

where N_{cell} is the number of cells in the stack, V_{Nernst} is the Nernst voltage, V_{act} is the voltage loss due to activation, V_{ohm} represents the ohmic losses and V_{conc} is the voltage loss due to concentration. The Nernst voltage was evaluated using:

$$V_{Nernst} = V_{cell}^{0} - \frac{R_g T}{2F} \ln\left(\frac{p_{H_2O}}{p_{O_2}^{0.5} p_{H2}}\right) \quad (6)$$

The term V_{cell}^{0} represents the standard cell potential, equal to 1.229 V. The standard cell potential is the ratio between the Gibbs free energy of water, equal to -237.14 kJ/mol, and $-2F$, where F is the Faraday constant, equal to 96,485.33 C/mol. R_g is the ideal gas constant, p_{H_2O}, p_{O_2} and p_{H_2} are, respectively, the water, oxygen and hydrogen partial pressures, T is the stack temperature. The activation, ohmic and concentration losses were evaluated using:

$$V_{act} = \frac{R_g T}{2F\alpha} \cdot \log\left(\frac{i_{dens}}{i_0}\right) \quad (7)$$

$$V_{ohm} = R_{ohm} \cdot i_{dens} \quad (8)$$

$$V_{conc} = \frac{R_g T}{2F} \cdot \log\left(1 - \frac{i_{dens}}{i_{lim}}\right) \quad (9)$$

where α is the charge transfer coefficient, i_{dens} is the current density, i_0 is the reaction exchange current density and i_{lim} is the maximum current density. The ohmic resistance of the fuel-cell stack is generally dependent on the stack temperature T and the membrane water content [33,34]. In particular, the membrane conductivity σ_{mem} per unit of length of the membrane thickness can be evaluated using:

$$\sigma_{mem} = (0.5139 \cdot \lambda_{mem} - 0.326) \cdot \exp\left[1268 \cdot \left(\frac{1}{303.15} - \frac{1}{T}\right)\right] \quad (10)$$

where λ_{mem} is the number of water molecules held per sulfonic acid group. Lastly, the membrane resistance was evaluated using:

$$R_{ohm} = \frac{t_{membrane}}{\sigma_{mem}} \quad (11)$$

The main properties of the fuel-cell stack considered in this work are shown in Table 3 according to data available from the literature and commercially available fuel-cell stacks. The single-cell voltage and the stack power density curves as functions of the current density of the fuel cell are represented in Figure 8.

Table 3. Main characteristics of the fuel-cell stack.

Parameters	Value	Unit
Number of cells	360	-
Cell active area	220	cm^2
Membrane thickness	100	µm
Anode gas diffusion layer thickness	200	µm
Cathode gas diffusion layer thickness	200	µm
Exchange current density	8×10^{-6}	A/cm^2
Max current density	1.4	A/cm^2
Charge transfer coefficient	0.5	-
Density of dry membrane	2000	kg/m^3
Equivalent weight of dry membrane	1.1	kg/mol

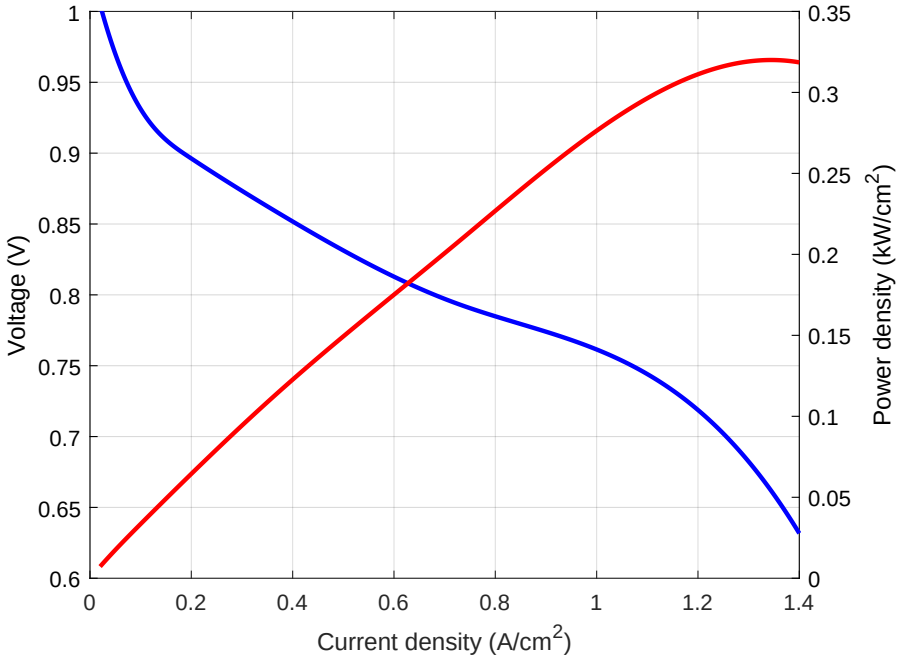

Figure 8. Cell voltage and power density curves as functions of current density.

3.2.2. H_2 Adduction System Model

The hydrogen adduction system consisted of a hydrogen source, represented by the hydrogen tank, where H_2 was stored at 700 bar and 298, 15 K, a pressure-reducing valve, which regulated the mass flow coming from the tank and maintained the pressure at the anode channels at the nominal value, and a recirculation system. From a numerical point of view, the following flows were defined: $q_{H_2}^{anode}$, which represented the hydrogen mass flow through the anode channels, $q_{H_2}^{react}$, which represented the hydrogen mass flow that reacted in the fuel cell, $q_{H_2}^{recirc}$, which represented the recirculated hydrogen mass flow, $q_{H_2}^{out}$, which referred to unused hydrogen that was not recirculated [35], and $q_{H_2}^{tank}$, which represented the hydrogen mass flow coming from the tank. A schematic representation of the hydrogen mass flows is shown in Figure 9. The hydrogen mass flow reacting in the fuel-cell anode was evaluated using:

$$q_{H_2}^{react} = \frac{N_{cell} i_{FC} MM_{H_2}}{2F} \tag{12}$$

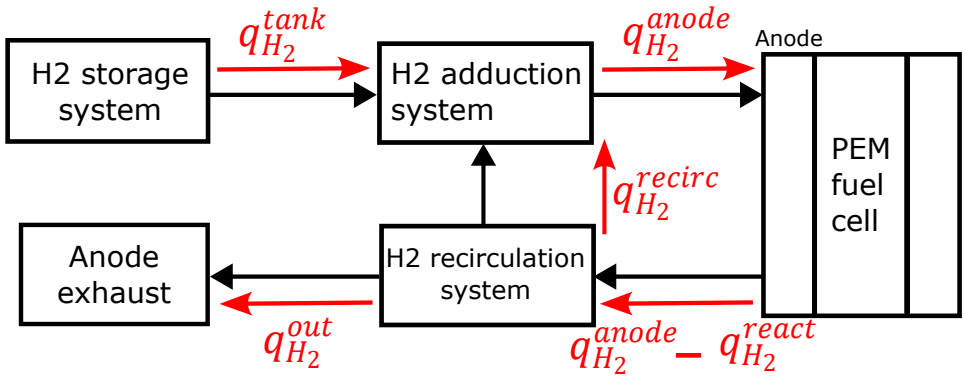

Figure 9. Schematic representation of the hydrogen mass flows in the hydrogen adduction system.

where MM_{H_2} is the H_2 molar mass and i_{FC} is the fuel-cell current. The hydrogen mass flow through the anode channels was evaluated using the following conservation relation:

$$q_{H_2}^{anode} = q_{H_2}^{tank} + q_{H_2}^{recirc} \tag{13}$$

As for $q_{H_2}^{tank}$, the hydrogen mass flow coming from the tank was regulated using the equations of a pressure-reducing valve, represented by a localized reduction in flow area. The value of the restriction area was regulated as a function of the pressure in the anode. Defined as a pressure range, when the hydrogen pressure at the anode channels was greater or equal than the nominal pressure, the local restriction area of the valve was at the minimum value. On the other hand, when the pressure was between $p_{H_2,nom}$ and $(p_{H_2,nom} - p_{range})$, the local restriction changed proportionally to the difference between the actual hydrogen pressure and its nominal value. When the pressure was lower than $(p_{H_2,nom} - p_{range})$, the local restriction area was at its maximum value. Fixing a volume of the anode, the hydrogen pressure variation was evaluated using the ideal gas law combined with the mass conservation law.

$$A_{restr} = \begin{cases} A_{restr_{max}} & if\, p_{H_2} < (p_{H_2,nom} - p_{range}) \\ A_{restr}(p_{H_2}) & if (p_{H_2,nom} - p_{range}) < p_{H_2} < (p_{H_2,nom}) \\ A_{restr_{min}} & if\, p_{H_2} > (p_{H_2,nom}) \end{cases} \tag{14}$$

3.2.3. Oxygen Adduction System Model

The oxygen mass flow reacting in the cathode was evaluated through the following equation:

$$q_{O_2}^{react} = \frac{N_{cell} i_{FC} M M_{O_2}}{4F} \tag{15}$$

The main element of the air adduction system is the compressor. The compressor was modeled as a controlled mass flow rate source. To control the air mass flow at the cathode, the reference parameter is the oxygen excess ratio (OER), which is defined as the ratio between the oxygen flow rate into the stack cathode and the oxygen flow rate that reacts at the cathode. To reach optimal value of efficiencies, the compressor must provide a certain value of OER [34,35] which depends on the stack properties, on the compressor and on the fuel-cell load. For simplicity, in this study, the OER was fixed at 2.5 and the compressor was regulated with a PI controller. The compressor is the auxiliary that requires more power by far; therefore, its power absorption was considered in the simulations by connecting an electric load to the DC bus. To evaluate the power absorbed by the compressor, its max isentropic efficiency was set equal to 60%. As for the oxygen pressure variation, it was evaluated using the same approach used for the hydrogen adduction system.

3.2.4. Battery Model

The battery was modeled using the dynamic equivalent circuit model [36] shown in Figure 10.

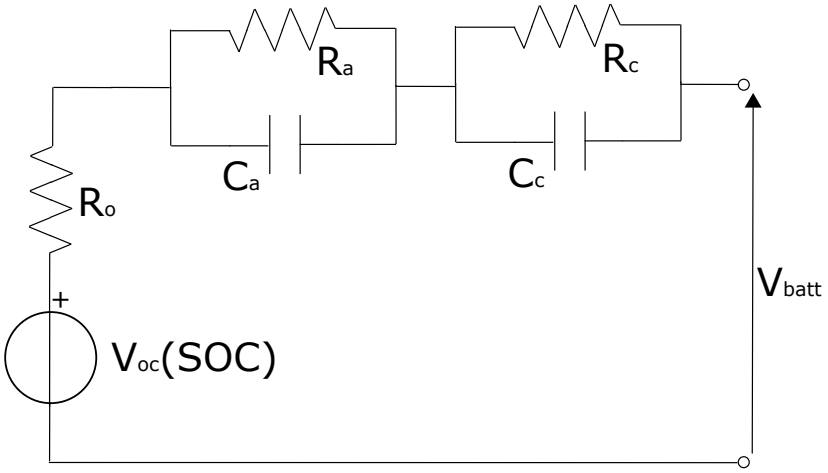

Figure 10. Equivalent dynamic circuit model of the battery pack.

where V_{OC} is the open circuit voltage, which was modeled as dependent on the state of charge (SOC) of the battery pack, R_o is the ohmic resistance, R_aC_a represents the activation dynamic and R_cC_c accounts for the concentration dynamic. The open circuit voltage was related to the SOC using:

$$V = V_{nom} \cdot \left(\frac{SOC}{1 - k(1 - SOC)}\right) \tag{16}$$

where k is a coefficient that depends on the battery pack. Figure 11 shows the open circuit voltage of the battery pack as function of the State of Charge. To evaluate the actual SOC of the battery pack, a simple Coulomb-counting strategy was used, neglecting more detailed models available in the literature. The reference equations are:

$$C_{used} = \int_{t_1}^{t_2} i_{batt} \, \mathrm{d}t \tag{17}$$

$$SOC = \frac{C_{nom} - C_{used}}{C_{nom}} \tag{18}$$

where C_{used} is the used capacity and C_{nom} is the nominal capacity. Since the on-board space availability of the considered tractor is limited, the sizing of the battery pack is characterized by severe constraints. Therefore, the battery pack capacity of the proposed fuel-cell tractor was limited to a reasonable value for a real application. The main properties of the battery pack and its numerical model are reported in Table 4.

Table 4. Battery pack nominal properties.

Battery Pack Properties	
Nominal open circuit voltage	240 V
Nominal capacity	6 kWh
Ohmic resistance	0.3 Ω
R_aC_a	30 s
R_cC_c	3000 s

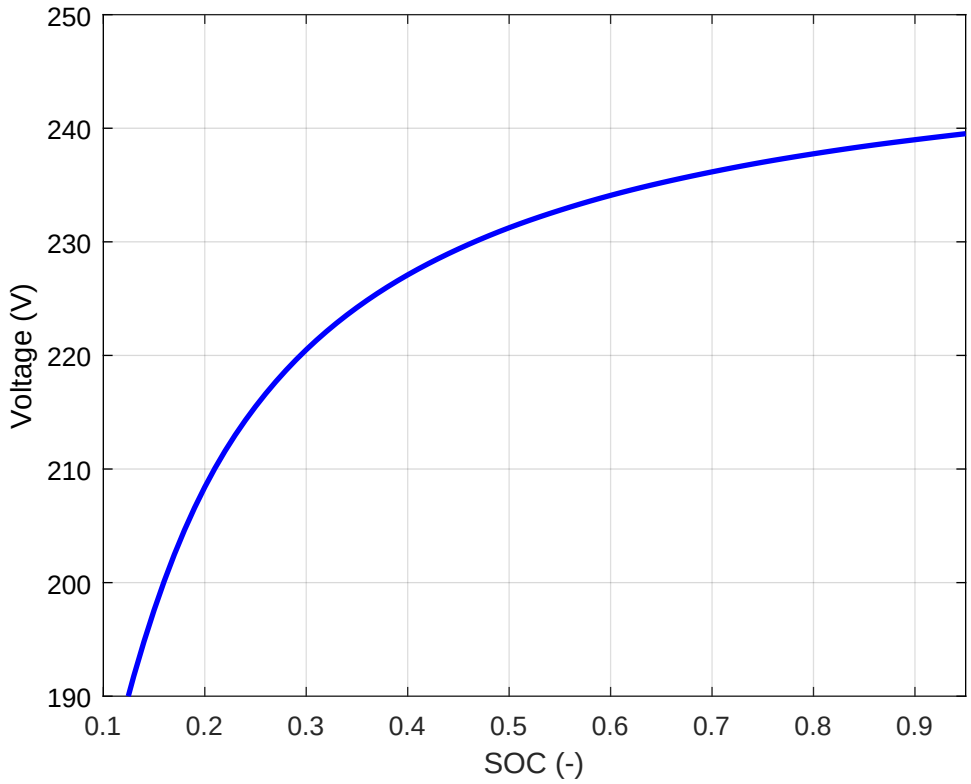

Figure 11. Battery pack voltage as function of the SOC.

3.2.5. DC–DC Converter Model

The DC–DC converter was modeled assuming its efficiency as a function of the input current (FC side current). Figure 12 shows the efficiency curve of the DC–DC converter. The DC–DC converter was regulated imposing its output current at the bus DC. The current was regulated as a function of the power request. To limit the gradient of the fuel-cell power output, the reference current command at the DC–DC was filtered with a transfer function, which mitigated the load dynamics.

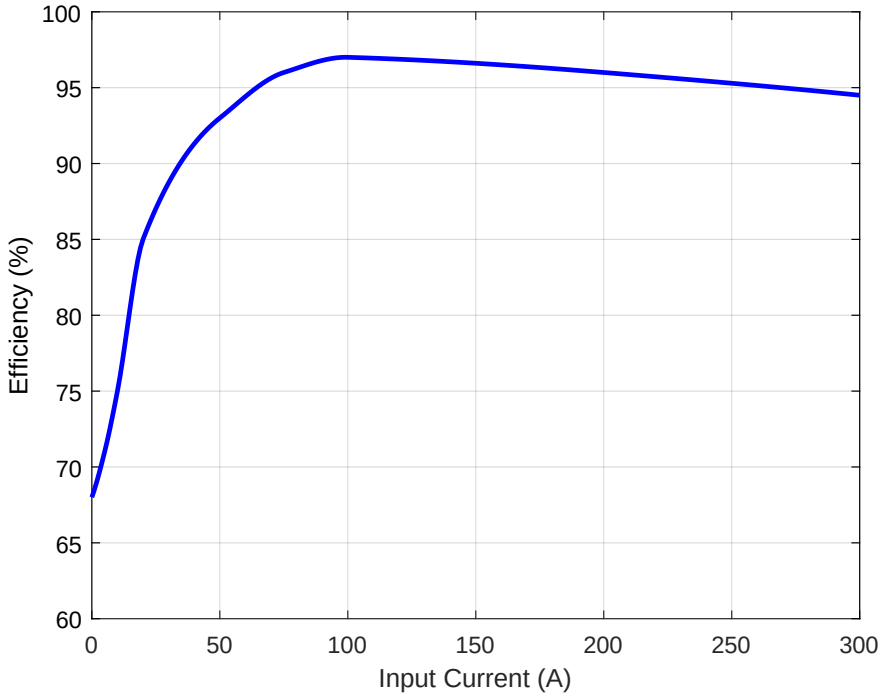

Figure 12. DC–DC efficiency curve as function of the input current.

4. Numerical Simulations

4.1. Powertrain Control Strategy

In contrast with the automotive sector, where the driver controls the target torque directly with the acceleration pedal, agricultural tractors mainly operate with a reference speed control [37]. In this case, the driver sets the desired engine speed, and the system computes the torque to reach and maintain the target speed. Therefore, during simulations, both the ICE and the EM were controlled by imposing the desired engine speed through a PI controller. The desired engine speed was recorded during the experimental monitoring of the work cycles. To achieve a plausible response of the powertrains during the simulations, the PI controller coefficients were calibrated according to the real behavior of the monitored tractor. As for the hybrid fuel-cell/battery tractor, the electric power required by the EM must be properly divided between the fuel cell and the battery pack. The energy-management strategy must limit the fuel-cell current slope during transients and preserve the battery pack SOC to accomplish a daily work task. Consequently, the battery pack must handle the fast-dynamic component of the load, while the fuel cell must follow the slow-dynamic component of the load. The element that permitted to control the power delivered by the fuel cell was the DC–DC converter [38]. The current reference command at the converter was evaluated using a function of the power request. The function was adjusted, with penalty factors, according to the actual SOC of the battery pack. When the BP SOC was low, the current reference was higher so that the excess power delivered by the fuel cell was used to recharge the batteries. Figure 13 shows a schematic representation of the hybrid fuel-cell/battery powertrain control strategy.

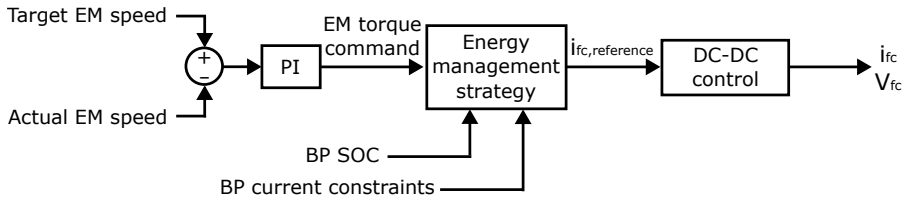

Figure 13. DC–DC efficiency curve as function of the input current.

During simulations, to propose a hypothetical precautionary approach to preserve the battery pack state of health (SOH) [39–41], the following constraints were applied:

- Max current during continuous discharging equal to 3C.
- Max current during instantaneous discharging equal to 5C.
- Max current during continuous charging equal to C.
- Max current during instantaneous charging equal to 1.5C.

4.2. Simulations Results

4.2.1. Acceleration Test

First, a peak power performance comparison was performed to evaluate the powertrain behavior under peak power demand conditions. Experimental data were recorded during an acceleration of 40 km/h on road with an attached trailer weighing about 2 tons. Experimental data were first compared with the simulation of the conventional vehicle, validating the numerical model, then were compared with the fuel-cell/battery powertrain. Results showed a slight increase in the acceleration time for the fuel-cell vehicle. The main reason for this was that the torque of the conventional diesel was greater compared to the electric motor torque at almost every rotational speed. Moreover, the constraints on the maximum discharge current of the BP had to be respected. However, the difference was little and thus the performances were similar. The simulation results are shown in Figure 14. During the simulations, the auxiliary loads were considered according to the experimental measurements.

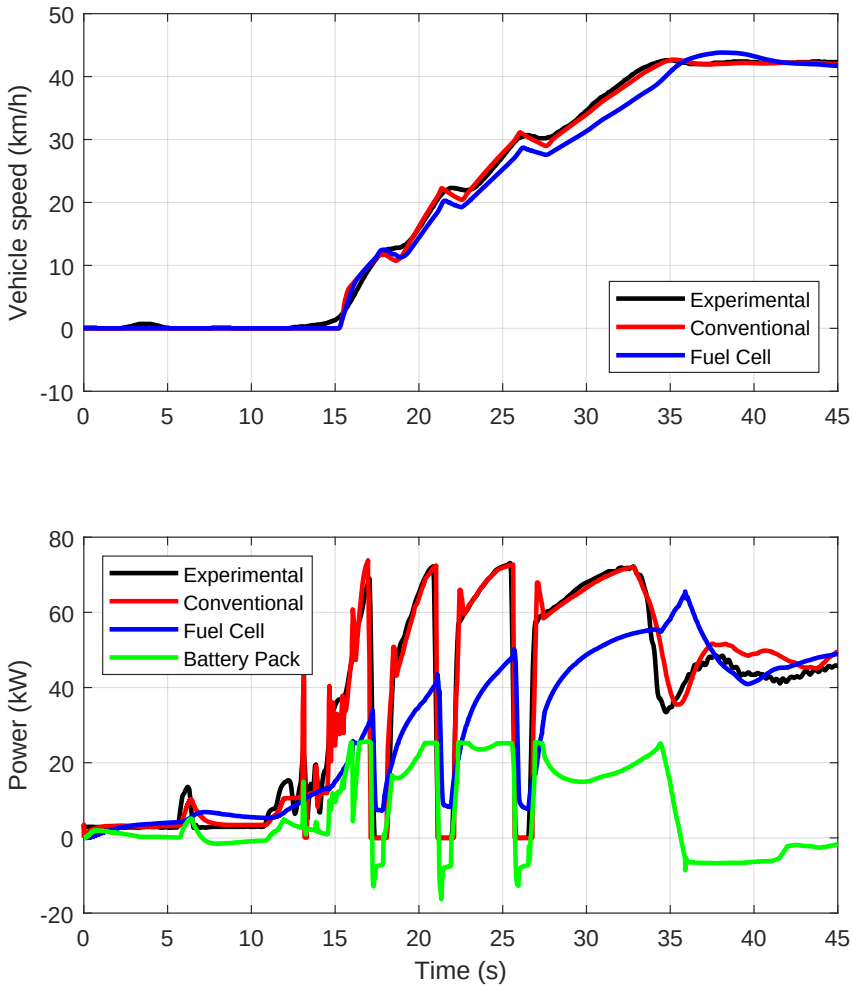

Figure 14. Acceleration test: Experimental vs. Simulations.

4.2.2. Work Cycle Simulation

Figures 15 and 16 show the simulation results in terms of vehicle speed, fuel economy, fuel cell and battery pack power and battery pack SOC. As for the vehicle speed, at some points the simulations were not able to replicate the experimental measured speed. This happened during vehicle turns, since to simulate properly that behavior, a 2D model was required. During field operations, the vehicle turned many times, as can be seen in Figure 6, especially in the weeding cycle, and this was because the vehicle was moving among orchard rows and had to turn every time it reached the end of the field. However, this problem does not significantly influence the results obtained. It is possible to highlight that the powertrain operated mainly in a charge-sustaining mode, since at the end of both simulations the battery pack SOC was approximately equal to the SOC level at the beginning. The most intense part in terms of power request can be identified during the road traveling from one field to another in the sprayer cycle. During this phase, the vehicle reached a traveling speed of about 40 km/h. During both the simulations, the BP current did not exceed the imposed safety limits. Looking at the power distribution between the fuel cell and the battery, it is possible to note that the battery handled the fast-dynamic component of the load, since its oscillations in the power output were more intense both in terms of slope and frequency. The fuel cell instead followed the slow-dynamic part of the load, since the transients in its power output were more gentle.

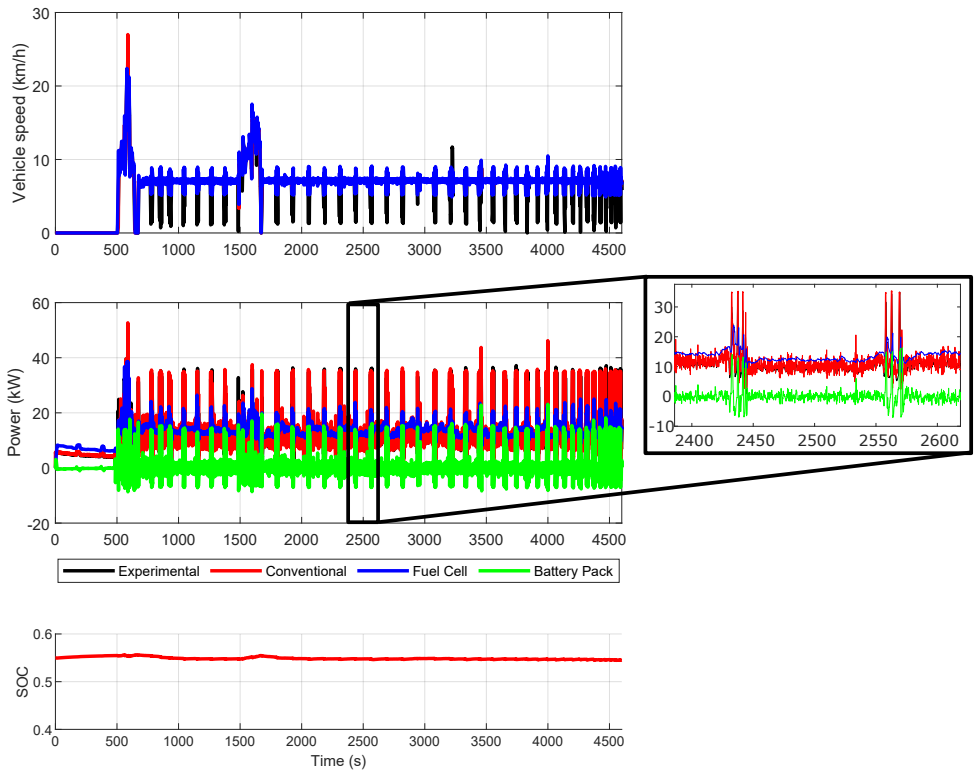

Figure 15. Simulation results for the weeding work cycle.

4.2.3. GHG Emission Comparison

To make a comparison between the conventional and fuel-cell/battery powertrains, an equivalent indicator was used. The fuel-cell/battery tractor in theory produces zero emissions locally. However, in the current state of the art, the production of hydrogen is far from being without emissions [21]. Therefore, a fair comparison between the traditional vehicle and the fuel-cell/battery vehicle in terms of emissions must consider the environmental impact also of the fuel-production processes. Following this premise, the attention focused on the well-to-wheels (WtW) CO_2 equivalent emissions of the fuel. According to [42], the WtW emission factors represent the emissions related to energy resource extraction, energy

carrier production, energy carrier distribution and energy conversion, and can be defined as the sum of the well-to-tank (WtT) emissions and the tank-to-wheels (TtW) emissions. According to studies available in the literature [43], the WtW CO_2 equivalent emission factors used in this study are reported in Table 5.

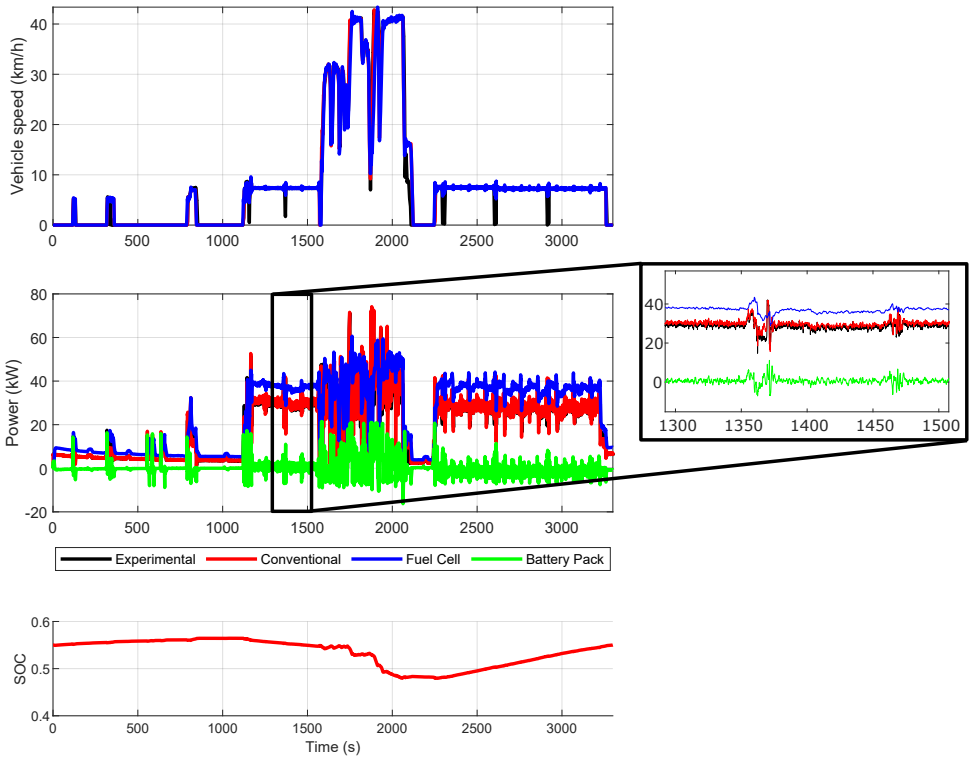

Figure 16. Simulation results for the sprayer work cycle.

Table 5. WtW equivalent CO_2 emission factors for Diesel and H_2.

Emission Source	WtW Emission Factor	Unit
Diesel	3.18	kg CO_2-eq./L
H_2	9.13	kg CO_2-eq./kg

Table 6 reports the simulation results for the fuel consumptions during the work cycles and the related equivalent CO_2 emissions. As for the sprayer work cycle, the fuel-cell tractor reduced the equivalent CO_2 emissions by about 44%, and this value reached about 55% for the weeding work cycle. The reduction of the equivalent CO_2 emissions was greater in this second case, since the mean power demand was lower, and therefore the conventional diesel tractor operated at a low overall efficiency. By contrast, the fuel cell operated at a greater efficiency, since the maximum efficiency for a PEM FC system is generally at low load [44].

Table 6. Simulation results for the total kg of equivalent CO_2 emissions.

	Sprayer Work Cycle		Weeder Work Cycle	
	Diesel	**Hydrogen**	**Diesel**	**Hydrogen**
Fuel consumption	5.35 L	1.049 kg	4.58 L	0.714 kg
kg CO_2 equivalent	17.02	9.58	14.56	6.52
Difference CO_2 eq.		−44%		−55%

5. Conclusions

To mitigate the environmental impact of agricultural tractors, several techniques have been explored in recent years. A possible solution is to replace diesel, partially or completely, with alternative fuels, such as biodiesel or biogas. Another technique is to hybridize the powertrain, substituting the traditional engine with a downsized engine and one or more electric machines. Moreover, to eliminate the local emissions deriving from combustion, pure electric tractors have been proposed. In this context of effort to reduce the environmental impact of agricultural machinery, fuel cells may play a relevant role. This work focused on the numerical investigation of a hybrid fuel-cell/battery powertrain for agricultural tractors. Compared with the aforementioned techniques, the following elements can be outlined:

- Fuel cells produce no harmful products at the exhaust; the only chemical by-product of the reaction between H_2 and O_2 is water.
- Fuel cell-powered vehicles can be refueled with hydrogen in a few minutes, as traditional diesel vehicles.

To define possible working scenarios for this kind of vehicle, data were collected through a CAN BUS analyzer on a tractor during its real operative use. To simulate the behavior of the powertrain, numerical models of its main components were developed and, from the experimental data, work cycles were derived and used for simulations. To properly split the electric power demand of the EM between the battery pack and the fuel cell, an energy-management strategy was defined. The simulations results can be summarized as follows:

- The fuel-cell/battery powertrain was able to accomplish the same tasks as the traditional vehicle.
- The fuel-cell/battery powertrain showed peak power performance very close to the traditional vehicle.
- Compared to diesel-powered agricultural tractors and considering the actual state-of-the-art hydrogen production methods, the fuel-cell/battery powertrain showed a reduction of about 50% of the equivalent CO_2 emissions accomplishing the same tasks, according to a WtW approach.

However, the reduction in terms of GHG emissions can be significantly increased with the development of greener hydrogen production systems. Thus, the adoption of a fuel-cell-powered powertrain could be a promising strategy, aiming at the reduction of GHG emissions. Future work might focus on the development of a scaled experimental test bench for hardware-in-the-loop (HIL) testing and on a deeper investigation of the energy-management strategy.

Author Contributions: Conceptualization, V.M., F.M. and A.S.; methodology, V.M., F.M. and A.S.; software, V.M., F.M. and A.S.; validation, V.M., F.M. and A.S.; formal analysis, V.M., F.M. and A.S.; investigation, V.M., F.M. and A.S.; data curation, V.M., F.M. and A.S.; writing−original draft preparation, V.M., F.M. and A.S.; writing−review and editing, V.M., F.M. and A.S.; visualization, V.M., F.M. and A.S.; supervision, V.M., F.M. and A.S. All authors have read and agreed to the published version of the manuscript.

Funding: This research received no external funding.

Institutional Review Board Statement: Not applicable.

Informed Consent Statement: Not applicable.

Data Availability Statement: Not applicable.

Conflicts of Interest: The authors declare no conflict of interest.

References

1. Platis, D.P.; Anagnostopoulos, C.D.; Tsaboula, A.D.; Menexes, G.C.; Kalburtji, K.L.; Mamolos, A.P. Energy Analysis, and Carbon and Water Footprint for Environmentally Friendly Farming Practices in Agroecosystems and Agroforestry. *Sustainability* **2019**, *11*, 1664. [CrossRef]
2. European Parliament—Council of the European Union. Regulation (EU). 2016/1628 of the European Parliament and of the Council of 14 September 2016 on requirements relating to gaseous and particulate pollutant emission limits and type-approval for internal combustion engines for non-road mobile machinery, amending Regulations (EU) No 1024/2012 and (EU) No 167/2013, and amending and repealing Directive 97/68/EC. *Off. J. Eur. Union* **2016**, *252*, 53–117.
3. Bacenetti, J.; Lovarelli, D.; Facchinetti, D.; Pessina, D. An environmental comparison of techniques to reduce pollutants emissions related to agricultural tractors. *Biosyst. Eng.* **2018**, *171*, 30–40. [CrossRef]
4. Tomic, M.; Savin, L.; Simikic, M.; Kiss, F.; Keselj, K.; Ivanisevic, M.; Ponjican, O.; Zoranovic, M.; Sedlar, A. Effects of biodiesel on changes in IC engine performances: A long-term experiment with farm tractors. *Fuel* **2021**, *292*, 120300. [CrossRef]
5. Owczuk, M.; Matuszewska, A.; Kruczyński, S.; Kamela, W. Evaluation of Using Biogas to Supply the Dual Fuel Diesel Engine of an Agricultural Tractor. *Energies* **2019**, *12*, 1071. [CrossRef]
6. Venkatesan, V.; Nallusamy, N. Pine oil-soapnut oil methyl ester blends: A hybrid biofuel approach to completely eliminate the use of diesel in a twin cylinder off-road tractor diesel engine. *Fuel* **2020**, *262*, 116500. [CrossRef]
7. Ettl, J.; Bernhardt, H.; Huber, G.; Thuneke, K.; Remmele, E.; Emberger, P. Evaluation of pure rapeseed oil as a renewable fuel for agricultural machinery based on emission characteristics and long-term operation behaviour of a fleet of 18 tractors. *SN Appl. Sci.* **2020**, *2*, 1711. [CrossRef]
8. Matuszewska, A.; Owczuk, M.; Zamojska-Jaroszewicz, A.; Jakubiak-Lasocka, J.; Lasocki, J.; Orliński, P. Evaluation of the biological methane potential of various feedstock for the production of biogas to supply agricultural tractors. *Energy Convers. Manag.* **2016**, *125*, 309–319. [CrossRef]
9. Simikic, M.; Tomic, M.; Savin, L.; Micic, R.; Ivanisevic, I.; Ivanisevic, M. Influence of biodiesel on the performances of farm tractors: Experimental testing in stationary and non-stationary conditions. *Renew. Energy* **2018**, *121*, 677–687. [CrossRef]
10. Mocera, F.; Somà, A. Analysis of a Parallel Hybrid Electric Tractor for Agricultural Applications. *Energies* **2020**, *13*, 3055. [CrossRef]
11. Mocera, F.; Martini, V.; Somà, A. Comparative Analysis of Hybrid Electric Architectures for Specialized Agricultural Tractors. *Energies* **2022**, *15*, 1944. [CrossRef]
12. Mocera, F.; Martini, V. Numerical Performance Investigation of a Hybrid eCVT Specialized Agricultural Tractor. *Appl. Sci.* **2022**, *12*, 2438. [CrossRef]
13. Dalboni, M.; Santarelli, P.; Patroncini, P.; Soldati, A.; Concari, C.; Lusignani, D. Electrification of a Compact Agricultural Tractor: A Successful Case Study. In Proceedings of the 2019 IEEE Transportation Electrification Conference and Expo (ITEC), Novi, MI, USA, 19–21 June 2019; IEEE: Piscataway, NJ, USA, 2019; pp. 1–6.
14. Mocera, F.; Martelli, S.; Costamagna M. Dynamic behaviour of a battery pack for agricultural applications. *IOP Conf. Ser. Mater. Sci. Eng.* **2022**, *1214*, 012032. [CrossRef]
15. Vogt, H.H.; de Melo, R.R.; Daher, S.; Schmuelling, B.; Antunes, F.L.M.; dos Santos, P.A.; Albiero, D. Electric tractor system for family farming: Increased autonomy and economic feasibility for an energy transition. *J. Energy Storage* **2021**, *40*, 102744. [CrossRef]
16. Melo, R.R.; Antunes, F.L.; Daher, S.; Vogt, H.H.; Albiero, D.; Tofoli, F.L. Conception of an electric propulsion system for a 9 kW electric tractor suitable for family farming. *IET Electr. Power Appl.* **2019**, *13*, 1993–2004. [CrossRef]
17. Li, Y.; Taghizadeh-Hesary, F. The economic feasibility of green hydrogen and fuel cell electric vehicles for road transport in China. *Energy Policy* **2022**, *160*, 112703. [CrossRef]
18. Duan, J.; He, Y.; Zhu, H.; Qin, G.; Wei, W. Research progress on performance of fuel cell system utilized in vehicle. *Int. J. Hydrog. Energy* **2019**, *44*, 5530–5537. [CrossRef]
19. Aguilar, P.; Groß, B. Battery electric vehicles and fuel cell electric vehicles, an analysis of alternative powertrains as a mean to decarbonise the transport sector. *Sustain. Energy Technol. Assess.* **2022**, *53*, 102624.
20. Madheswaran, D.K.; Jayakumar, A.; Varuvel, E.G. Recent advancement on thermal management strategies in PEM fuel cell stack: a technical assessment from the context of fuel cell electric vehicle application. *Energy Sources Part A* **2022**, *44*, 3100–3125. [CrossRef]
21. Ji, M.; Wang, J. Review and comparison of various hydrogen production methods based on costs and life cycle impact assessment indicators. *Int. J. Hydrog. Energy* **2021**, *46*, 38612–38635. [CrossRef]
22. Xu, X.; Zhou, Q.; Yu, D. The future of hydrogen energy: Bio-hydrogen production technology. *Int. J. Hydrog. Energy* **2022**, *47*, 33677–33698. [CrossRef]
23. Das, A.; Peu, S.D. A Comprehensive Review on Recent Advancements in Thermochemical Processes for Clean Hydrogen Production to Decarbonize the Energy Sector. *Sustainability* **2022**, *14*, 11206. [CrossRef]
24. Thounthong, P.; Rael, S.; Davat, B. Energy management of fuel cell/battery/supercapacitor hybrid power source for vehicle applications. *J. Power Sources* **2009**, *193*, 376–385. [CrossRef]
25. Chen, H.; Zhao, X.; Zhang, T.; Pei, P. The reactant starvation of the proton exchange membrane fuel cells for vehicular applications: A review. *Energy Convers. Manag.* **2019**, *182*, 282–298. [CrossRef]

26. Zhao, X.; Wang, L.; Zhou, Y. Pan, B.; Wang, R.; Wang, L.; Yan, X. Energy management strategies for fuel cell hybrid electric vehicles: Classification, comparison, and outlook. *Energy Convers. Manag.* **2022**, *270*, 116179. [CrossRef]
27. Ahluwalia, R.K.; Wang, X.; Star, A.G.; Papadias, D.D. Performance and cost of fuel cells for off-road heavy-duty vehicles. *Int. J. Hydrog. Energy* **2022**, *47*, 10990–11006. [CrossRef]
28. Tritschler, P.J.; Bacha, S.; Rullière, E.; Husson, G. Energy Management Strategies for an embedded Fuel Cell System on Agricultural Vehicles. In Proceedings of the XIX International Conference on Electrical Machines—ICEM 2010, Rome, Italy, 6–8 September 2010.
29. Yang, H.; Sun, Y.; Xia, C.; Zhang, H. Research on Energy Management Strategy of Fuel Cell Electric Tractor Based on Multi-Algorithm Fusion and Optimization. *Energies* **2022**, *15*, 6389. [CrossRef]
30. Voss, W. *A Comprehensible Guide to Controller Area Network*; Copperhill Technologies Corporation: Greenfield, MA, USA, 2005.
31. Voss, W. *A Comprehensible Guide to J1939*; Copperhill Technologies Corporation: Greenfield, MA, USA, 2008.
32. Golverk, A.A. The Method for Development of a Diesel Engine Universal Performance Map. *SAE Int. J. Fuels Lubr.* **1994**, *103*, 1041–1048.
33. Huang, Z.; Shen, J.; Chan, S.H.; Tu, Z. Transient response of performance in a proton exchange membrane fuel cell under dynamic loading. *Energy Convers. Manag.* **2020**, *226*, 113492. [CrossRef]
34. Cruz Rojas, A.; Lopez Lopez, G.; Gomez-Aguilar, J.F.; Alvarado, V.M.; Sandoval Torres, C.L. Control of the Air Supply Subsystem in a PEMFC with Balance of Plant Simulation. *Sustainability* **2017**, *9*, 73. [CrossRef]
35. Wang, Y.; Sun, Z.; Chen, Z. Energy management strategy for battery/supercapacitor/fuel cell hybrid source vehicles based on finite state machine. *Appl. Energy* **2019**, *254*, 113707. [CrossRef]
36. Vergori, E.; Mocera, F.; Somà, A. Battery Modelling and Simulation Using a Programmable Testing Equipment. *Computers* **2018**, *7*, 20. [CrossRef]
37. Wu, Z.; Xie, B.; Li, Z.; Chi, R.; Ren, Z.; Du, Y.; Inoue, E.; Mitsuoka, M.; Okayasu, T.; Hirai, Y. Modelling and verification of driving torque management for electric tractor: Dual-mode driving intention interpretation with torque demand restriction. *Biosyst. Eng.* **2019**, *182*, 65–83. [CrossRef]
38. Vural, B.; Boynuegri, A. R.; Nakir, I.; Erdinc, O.; Balikci, A.; Uzunoglu, M.; Gorgun, H.; Dusmez, S. Fuel cell and ultra-capacitor hybridization: A prototype test bench based analysis of different energy management strategies for vehicular applications. *Int. J. Hydrog. Energy* **2010**, *35*, 11161–11171. [CrossRef]
39. Di Ilio, G.; Di Giorgio, P.; Tribioli, L.; Bella, G.; Jannelli, E. Preliminary design of a fuel cell/battery hybrid powertrain for a heavy-duty yard truck for port logistics. *Energy Convers. Manag.* **2021**, *243*, 114423. [CrossRef]
40. Mocera, F.; Somà, A. Working Cycle requirements for an electrified architecture of a vertical feed mixer vehicle. *Procedia Struct. Integr.* **2018**, *12*, 213–223. [CrossRef]
41. Mocera, F.; Vergori, E.; Soma, A. Battery Performance Analysis for Working Vehicle Applications. *IEEE Trans. Ind. Appl.* **2020**, *56*, 644–653. [CrossRef]
42. Nordelöf, A.; Messagie, M.; Tillman, A. M.; Ljunggren Söderman, M.; van Mierlo, J. Environmental impacts of hybrid, plug-in hybrid, and battery electric vehicles—what can we learn from life cycle assessment? *Int. J. Life Cycle Assess.* **2014**, *19*, 1866–1890. [CrossRef]
43. Buberger, J.; Kersten, A.; Kuder, M.; Eckerle, R.; Weyh, T.; Thiringer, T. Total CO2-equivalent life-cycle emissions from commercially available passenger cars. *Renew. Sust. Energ. Rev.* **2022**, *159*, 112158. [CrossRef]
44. Lohse-Busch, H.; Stutenberg, K.; Duoba, M.; Liu, X.; Elgowainy, A.; Wang, M.; Wallner, T.; Richard, B.; Christenson, M. Automotive fuel cell stack and system efficiency and fuel consumption based on vehicle testing on a chassis dynamometer at min 18 °C to positive 35 °C temperatures. *Int. J. Hydrog. Energy* **2020**, *45*, 861–872. [CrossRef]